Bioimaging and Quantum Sensing Using NV Centers in Diamond Nanoparticles

Yuen Yung Hui, Chi-An Cheng, Oliver Y. Chen and Huan-Cheng Chang

Abstract Diamond nanoparticle hosting negatively-charged nitrogen vacancy (NV^-) center has unique chemical, optical and spin properties in a wide range of nanotechnology applications. For instance, diamond nanoparticles containing NV centers have been well-known as Fluorescent NanoDiamond (FND) for fluorescence imaging. Recently the NV^- center has been applied for nanothermometry. In this chapter we are going to discuss the recent advances of the NV^- center for bioimaging and quantum sensing.

Keywords Bioimaging · Fluorescent nanodiamond · Nitrogen vacancy center · Optically detected magnetic resonance · Quantum sensing

1 Introduction

Fluorescent NanoDiamond (FND) containing negatively-charged nitrogen vacancy (NV^-) center has recently attracted much attention in a wide range of nanotechnology applications [1]. FND owes its quantum properties to NV^- center's unique triplet ground state, whose spin not only can be optically detected but also optically manipulated [2]. Most remarkably, a NV^- center, locked within the diamond matrix, retains these quantum properties and has a spin coherence time as long as 10 ms even at ambient environments [3]. Combined with nanodiamond's chemical inertness and biocompatibility, FND makes the perfect candidate to import quantum physics into biology and opens up new territories and possibilities for bioimaging [4]. We are going to focus on the recent advance of the NV centers hosting in diamond nanoparticle [5] in this chapter, since the NV center in bulk diamond crystal has been recently comprehensively reviewed by Schirhagl et al. [1]. The

Y.Y. Hui (✉) · C.-A. Cheng · O.Y. Chen · H.-C. Chang (✉)
Institute of Atomic and Molecular Sciences, Academia Sinica, Taipe 106, Taiwan
e-mail: yyhui@pub.iams.sinica.edu.tw

H.-C. Chang
e-mail: hchang@gate.sinica.edu.tw

N. Yang et al. (eds.), *Carbon Nanoparticles and Nanostructures*,
Carbon Nanostructures, DOI 10.1007/978-3-319-28782-9_4

basic properties of a NV center are elaborated in Sect. 2. Then we will discuss the emerging technologies of the NV^- center for bioimaging and quantum sensing in Sects. 3 and 4 respectively. We also provide the perspective of the center in the final section.

2 Unique Properties of Negative Nitrogen-Vacancy (NV^-) Center

2.1 Electronic Structure of NV Center

A NV center is composed of a carbon vacancy site adjacent to one substitutional nitrogen atom. An imaginary line that passes through the vacancy site and the nitrogen atom is a symmetry axis, assuming along ⟨111⟩ direction (Fig. 1). The symmetry of the NV center belongs to the C_{3v} point group. In diamond, carbon's valence electrons occupy the sp^3 hybridized orbitals. In defectless diamond, all the orbitals are completely filled with 2 electrons. If one carbon atom were to be removed from the diamond matrix, it effectively removes 4 valence electrons along with +4-charged ion core. This defect, known as GR1 center, remains charge neutral and creates 4 holes in the previously completely filled orbitals. Moreover, if one of the carbon atoms near the vacancy is replaced by a nitrogen atom, then the one extra valence electron from a nitrogen atom will fill out one hole. This neutral NV defect center, known as NV^0, has 3 holes and zero net charge [6]. Furthermore, if this defect center traps one extra electron from an electron-rich source, possibly nearby defects or crystal surface [1], then another hole is annihilated. This NV^- center now has 2 holes and net charge of −1. Both neutral and negative NV center in diamond share similar optical properties for bioimaging (like red fluorescence and photostability), but only the negative NV center has demonstrated unique spin properties for quantum sensing.

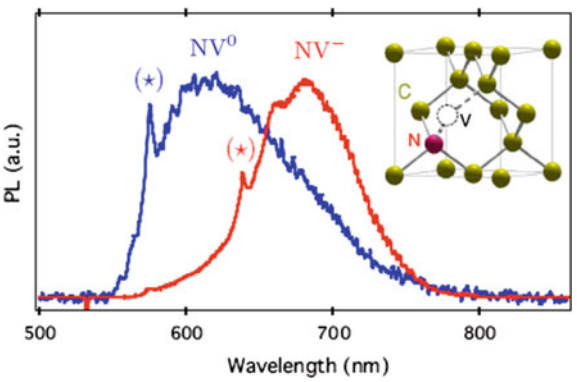

Fig. 1 PL spectra of NV^0 center and NV^- center. The zero-phonon line of NV^0 center and NV^- center are 575 nm and 637 nm respectively. *Inset*: Structure of NV center in diamond lattice. (Reprinted from Rondin et al. [7])

2.2 Common Optical Properties of NV Center

The NV^0 center and the NV^- center produce red fluorescence with zero phonon line (ZPL) at 576 nm and 637 nm respectively [7], shown in Fig. 1. Both ZPLs are accompanied with broad phonon sidebands red-shifted by about 50 nm. (It has further found that the NV^0 center can be converted to NV^- center in diamond by annealing in oxygen environment [7, 8].) Since both NV centers are hosted in the diamond lattice, they are photostable, compared with other organic fluorophores [9]. Apart from the excellent photostability, nanodiamond is biocompatible with animal [10–13]. Hence, the NV centers in nanodiamond enable long-term fluorescence tracking in biological systems.

2.3 Unique Spin Properties of NV^- Center

The NV^- center in diamond has unique spin properties, because of the triplet ground state and excited state. The experimental and theoretical constructions for the energy state diagram have been recently reviewed [14, 15]. The simplified energy level diagram is displayed in Fig. 2, which can describe the photo-physics of the NV^- center. The NV^- center is treated as a three-level system with a triplet ground state $^3A_2$, a triplet excited state ^3E and intermediate singlet states. The energy separation between the triplet ground state and the triplet excited states is 1.945 eV, which corresponds to the zero phonon line of NV^- center at 637 nm. Both triplet states of the NV^- center show a zero-field splitting among the spin sublevels with $m_s = 0$ and $m_s = \pm 1$ respectively. The energy splitting of the ground

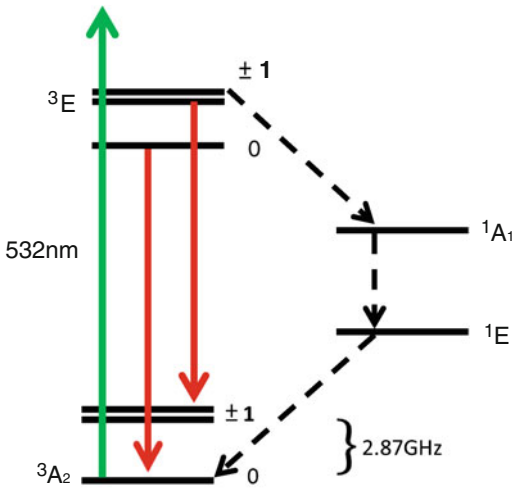

Fig. 2 Energy level diagram for a NV^- center

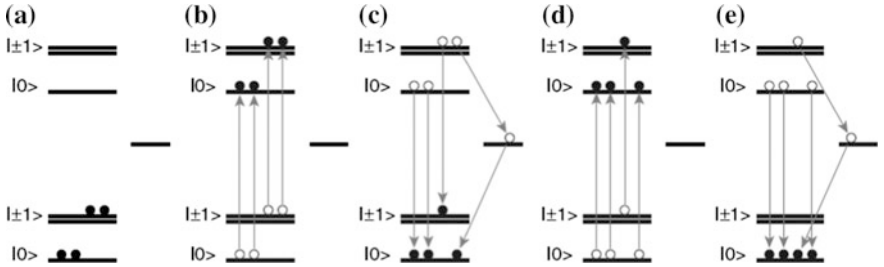

Fig. 3 Schematic representation for the polarization mechanism of a NV^- center. (Reprinted from Bradac et al. [2])

state (without an external field) has been measured as 2.87 GHz which corresponds to the microwave excitation.

Moreover, the spin-state of a NV^- center can be optically polarized [16]. In other words, optical excitation can induce a non-Boltzmann steady-state spin alignment of the NV^- center in the ground state, and hence the $m_s = 0$ sublevel of the ground state can be preferentially populated. We will illustrate the polarization mechanism in Fig. 3 [2]. Initially the NV^- center is unpolarized, wherein the $m_s = 0$ and $m_s = \pm 1$ sublevels of the ground state are equally populated in Fig. 3a. When the NV^- center is excited by a green laser, the population in the $m_s = 0$ and $m_s = \pm 1$ sublevels of the ground state shifts to the corresponding sublevels of the excited state. The optical transition is spin-conserving, and hence the spin number conserves in Fig. 3b. Furthermore, the population in the excited state can return to the ground state either by radiative transition or by non-radiative transition. The radiative transition produces the emission of red photons with ZPL at 637 nm. However, the non-radiative transition involving the singlet state is not necessarily spin-conserving. The dominant non-radiative decay path travels from the $m_s = \pm 1$ sublevel of the excited state to the singlet intermediate state and eventually to the $m_s = 0$ sublevel of the ground state in Fig. 3c [17]. A few optical cycles can polarize the NV^- center to its $m_s = 0$ sublevel, shown in Fig. 3e. The spin-state of the NV center is said to be polarized, and hence the population distribution of the unpolarized NV^- center is different from the polarized NV^- center.

2.4 Optically Detected Magnetic Resonance (ODMR)

The population for the sublevel of the ground state in the NV^- center can be optically detected and manipulated by a resonant microwave of 2.87 GHz [18]. For example, an NV^- center is polarized with the $m_s = 0$ sublevel of the ground state.

The application of a resonant microwave increases the population for the $m_s = \pm 1$ sublevel of the ground state, similar to magnetic resonance. If the NV^- center is further probed with a green laser, the fluorescence intensity will decrease because of the non-radiative decay via the intermediate singlet state. Hence, the fluorescence intensity from the NV^- center is correlated with the population for the sublevel of the ground state. The fluorescence intensity from carries the information of spin state of the NV^- center. We can slowly sweep an auxiliary microwave over the diamond sample to detect the spin state of the NV^- center optically, and obtain an optically detected magnetic resonance (ODMR) spectrum.

When the NV^- center is polarized and the $m_s = 0$ sublevel of the ground state is preferentially occupied, the center produce maximum fluorescence intensity. On the other hand, when the center is unpolarized, the $m_s = 0$ and $m_s = \pm 1$ sublevels of the ground state are both equally populated. Under optical excitation, the center will undergo the non-radiative decay via the transition between $m_s = \pm 1$ to the singlet state and so its fluorescence intensity is 20–30 % lower than the maximum intensity. This ODMR effect is a characteristic of the NV^- center, which has only been observed for a handful of molecules and defects.

2.5 *Production of NV Centers in Diamond Nanoparticles*

In 2001, single NV^- center in diamond nanoparticles was produced for quantum communication [19]. Later Yu et al. demonstrated that diamond nanoparticles hosting multiple NV centers are applicable for cellular fluorescence imaging [20]. Since then, there have been a large number of researches aiming to produce small and bright FND [21–24]. (For sake of bioimaging application, the FND particle should be small, and contain as many NV centers as possible.) NV centers can be created by irradiating diamond nanoparticles with high energy particles (electrons, neutrons, protons, helium ions) and followed by vacuum annealing at 600–800 °C. High-energy particle irradiation forms vacancies in the diamond structure, then vacuum annealing allows these vacancies to migrate and to be trapped by nitrogen atoms to form NV centers. Mass production of FND has also been developed for biomedical applications since 2008 [25]. More specifically, synthetic type Ib diamond powders (with mean sizes of 35 and 140 nm respectively) typically contain 100 ppm of atomically dispersed nitrogen atoms as the major internal impurity. Chang et al. applied 40 keV He^+ ion bombardment at a dose of about 1×10^{13} ions cm^{-2} on synthetic type Ib diamond powders for the creation of radiation damage. It is noted that He^+ ion owns some merits as the irradiation source. Firstly, helium atoms are chemically inert, and embedding these atoms in a diamond lattice does

not significantly change the photophysical properties of the FNDs. Secondly, helium atoms possess remarkably high damage efficiency which reduces the dosage for ion irradiation. (For instance, a single 40 keV He^+ ion can create 40 vacancies in diamond, in contrast to the 0.1 and 13 vacancies generated by 2 meV e^- and 3 meV H^+ ion respectively.)

Based on density functional theory, the NV center concentration was predicted to increase nonlinearly with the crystal size [26]. The probability of producing NV centers was less than 5 % in High-Pressure-High-Temperature nanodiamond with 30 nm in size, due to the vacancy annihilation at the surface. In addition, quantitative analysis using Monte Carlo simulations for the size effect was performed [27]. The predicted probability of forming NV centers in nanodiamond with 5 nm in size was about 4.5 and 25 times lower than 20 nm and 55 nm respectively. Although the feasibility of producing NV centers in smaller ND particles is predicted to be low, many efforts have been contributed to produce ultra-small nanodiamond for bio-imaging. For example, Boudou et al. reduced the size of FND by ball milling [28, 29]. The procedure was shown in Fig. 4. The starting material was microdiamond instead of nanodiamond, because it offered a long vacancy migration path, which significantly increases the probability of vacancy trapping by nitrogen atom. Briefly, microdiamond powders were irradiated in a linear particle accelerator consisting of an electron beam with energy of 10 meV. Then, the irradiated particles were annealed at 750 °C to form fluorescent microdiamonds. The authors further applied nitrogen jet milling and ball milling in order to further convert fluorescent microdiamonds into smaller particles. The final size of the milled particles was smaller than 10 nm [29]. On the other hand, the size of the nanodiamond can also be reduced by air oxidation [30, 31]. In addition, Rabeau et al. produced NV^- centers in diamond nanocrystals by chemical vapour deposition (CVD). The NDs are grown directly on quartz cover slips in a microwave plasma CVD reactor, during when the substrate temperature was maintained at 800 °C. Single NV^- centers are observed in the resultant nanocrystals [32].

Furthermore, Mich et al. reported a microwave plasma-assisted chemical vapor deposition diamond growth technique on (111)-oriented bulk diamond substrates, and successfully produced perfect alignment of as-grown NV centers along a single crystallographic direction [33]. Now the aligned NV centers were formed by the incorporation of nitrogen atoms in the (111) growth surface and then followed by the neighboring vacancy on top. Meanwhile, Edmonds et al. produced NV center with two orientations, instead of four, by chemical vapour deposition [34]. (There are four possible orientations of the NV centers in the diamond crystal.) The achieved homogeneity of the grown NV centers in bulk diamond is anticipated to benefit quantum information and metrology applications. Multiple NV centers with a preferential direction in nanodiamond can impose significant impact to bioimaging and magnetometry [3, 35].

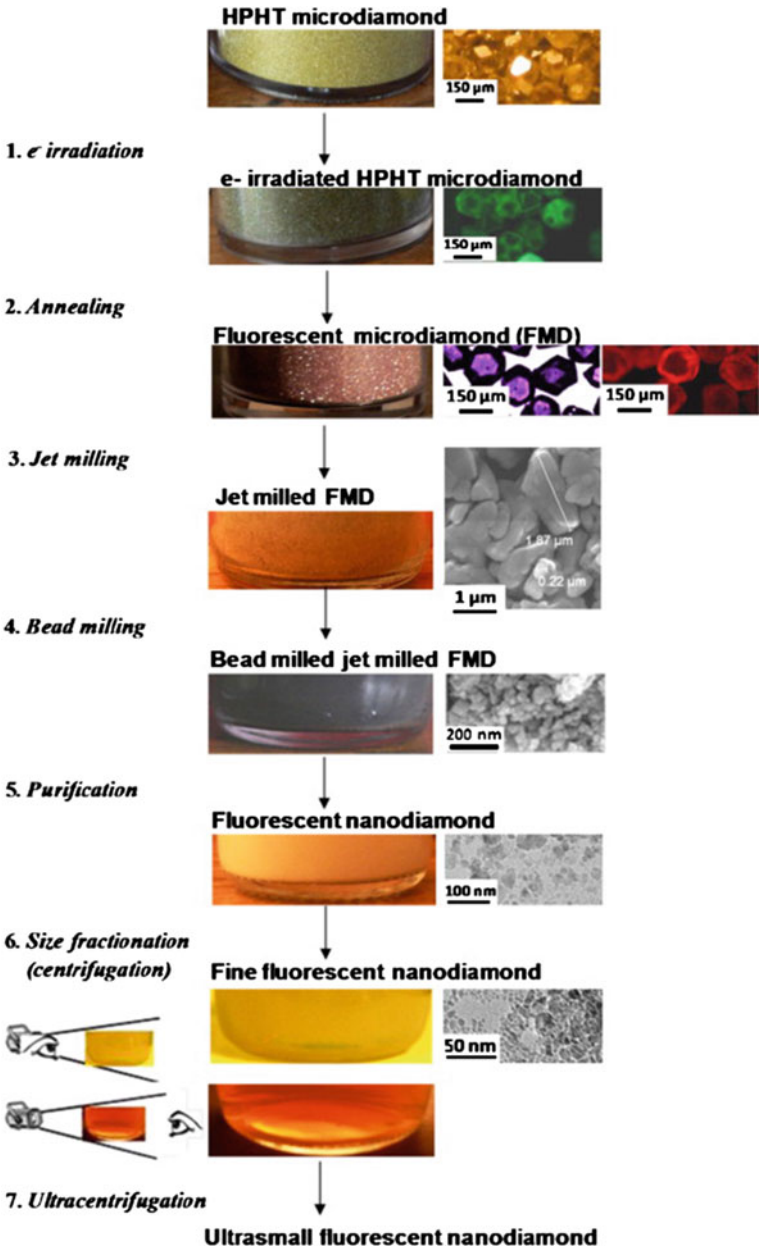

Fig. 4 Flow chart illustrating for the FND preparation. Sample images obtained at each step are provided in the center column. In contrast to previously synthesized nanodiamonds, a dispersion of fine fluorescent nanodiamonds in water is translucent and appears *orange* with a *white lamp* in the *inset* on the *left-hand side*. Microscope images on the *right-hand column*. (Reprinted from Boudou et al. [29])

3 Emerging Technologies for Bioimaging

3.1 Fluorescence Imaging for In Vivo Long-Term Tracking in Small Animals

FND contains a high concentration of NV defects as fluorescent centers. It has emerged as a promising new nanoparticle platform for bioimaging applications [36–38]. As illustrated in the previous section, NV centers emit bright and stable far red fluorescence when exposed to green-yellow light. No degradation of the fluorescence intensity has been observed even after prolonged laser irradiation of individual FND particles at room temperature [39]. Extreme photostability of FND is an outstanding feature of FND to be distinguished from other fluorophores and to become a potent cellular marker. Apart from the excellent photostability, good biocompatibility is another merit of FND for fluorescence imaging in biological systems.

For in vitro biological applications, FND has been demonstrated to be a long-term cell marker [40]. For instance, the cell division of FND-labeled HeLa cells can be observed up to 6 days (Fig. 5). The FND-labeled cells are allowed to be tracked within a longer period of time, once a large amount of FND is applied to label the cells. For in vivo studies, FND-cell labeling technique has been applied to model organisms like *Caenorhabditis elegans* [11, 41]. Recently, FND has also been applied to study another model organism, *Drosophila melanogaster* [42]. During the development of the *Drosophila* embryo, a single layer of nuclei is formed underlying the plasma membrane. Then cellularization begins with furrows of plasma membrane introgressing between adjacent nuclei and enclosing each nucleus to form a layer of outer cells (blastoderm cells) and a single large syncytial yolk cell (Fig. 6). Based on the accessibility of these outer cells for live imaging and the ability to manipulate cellular processes both genetically and pharmacologically (i.e. by injection of drugs into the syncytium), the cellularization serves as an outstanding model system to investigate the complex cellular processes underlying embryonic development. The authors demonstrated that the FND enables in vivo imaging of the embryos [42]. Most of the FND were located at the periphery of the cell where the membrane furrow was introgressing (Fig. 6c). Taking

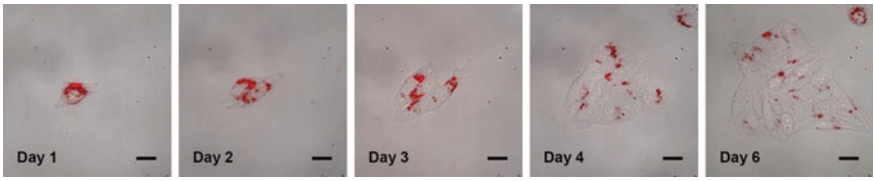

Fig. 5 Tracking for cell division of FND-labeled HeLa cells by DIC/epi-fluorescence microscopy. The tracking was conducted for up to 6 days of post-labeling incubation. Scale bars are 20 μm. (Reprinted from Fang et al. [40])

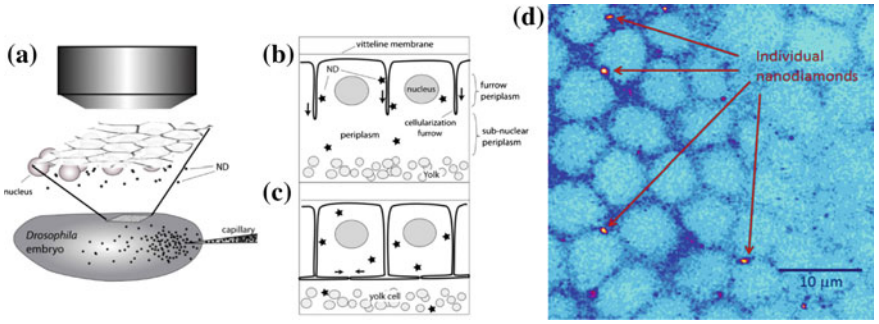

Fig. 6 **a** Schematic of the micro-injection of nanodiamonds into the Drosophila embryo. Early **b** and late **c** Stage 5 embryos showing the cellularization furrows introgressing between nuclei, which invade the yolk-free periplasm during the later syncytial divisions indicated as *arrows* in **b**. Nanodiamonds that have diffused into the yolk-free periplasm can become internalized in the blastoderm cells at the completion of Stage 5. **d** Scanning confocal fluorescence image of individual nanodiamonds in the blastoderm cells during Stage 5 of development. The image shows the auto-fluorescence from the introgressing cellularization furrows defining each blastoderm cell as well as the strong fluorescent signal from individual nanodiamonds which in the majority of cases is localized to the cell periphery. (Reprinted from Simpson et al. [42])

advantage of the photostability of the NV^- center in FND, the authors did the single particle tracking of individual FND particles in the blastoderm cells of developing *Drosophila* embryos. Since the FND fluorescence could be clearly distinguished from the embryo autofluorescence, the dynamics of individual FND particles were easily probed. The authors first took wide-field fluorescence images of the embryo which were divided into two sections. The first section of images was measured at the level of the nuclei and ingressing furrow, and the second section of images was measured in the periplasm underlying the nuclei. The results showed that the transport mechanisms of FND in the furrow were similar to the sub-nuclear periplasm.

3.2 *Time-Gated Fluorescence Imaging and Fluorescence Lifetime Imaging*

During fluorescence imaging, the biological systems always produce an autofluorescence background which interferes the FND signal and deteriorates the signal-to-background ratio. Another parameter that can be manipulated to enhance the image contrast of single FND in biological environments is the relatively long-lived fluorescence lifetime of the NV center, i.e. 11.6 ns in bulk diamond [43]. The lifetime of NV centers is substantially longer than that of cell and tissue autofluorescence (about 1–4 ns). Time-gating fluorescence imaging and Fluorescence Lifetime imaging (FLIM) can eliminate the autofluorescence background signal during fluorescence detection.

For instance, FND was non-covalently coated with YLCs (yolk lipoprotein complexes) by physical adsorption. Then the YLC-conjugated FND (YLC-FNDs) was micro-injected into the intestine of the *Caenorhabditis elegans* [41] and monitored temporally and spatially in vivo with the combined FND-FLIM technique. Before time-gating, the fluorescence signal from FND could not be easily differentiated from the background, mainly contributed by the intestinal cells (Fig. 7c). In contrast, the YLC-FNDs could be identified easily in the FLIM image, which takes advantage of FND's uniquely long fluorescence lifetime (Fig. 7d). Moreover, the background signal is significantly reduced after gating the fluorescence signal at the lifetime longer than 10 ns (Fig. 7e). To demonstrate that FND is biocompatible even when performing long-term in vivo tracking, the authors microinjected the GFP::YLC (a GFP molecule fused to YLC) -FND particles into the distal arm of the adult gonad. After tracing the particles for about 12 h, the GFP::YLC-FND-targeted oocytes were observed to grow into mature oocytes, suggesting that the oocytes with FND nanoparticles could develop normally without any influence.

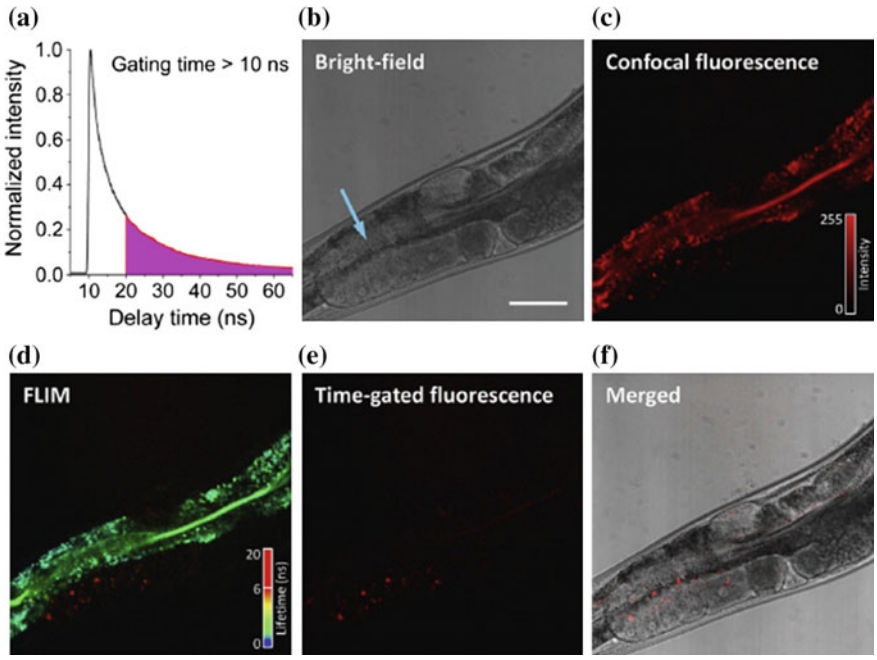

Fig. 7 Observation of GFP::YLC-FNDs in *C. elegans* by FLIM. **a** A fluorescence decay time trace of 100-nm FNDs suspended in water. The area *shaded in magenta* represents the fluorescence signal collected at the gating time (s) longer than 10 ns. **b** Bright-field, **c** confocal fluorescence, **d** FLIM, **e** time-gated fluorescence image at gating time > 10 ns, and **f** merged bright-field and time-gated fluorescence images of a worm microinjected with GFP::YLC-FNDs at the distal gonad. A *blue arrow* indicates the site of injection. Anterior is *left* and dorsal is up in all figures. Scale bar is 50 mm. (Reprinted from Kuo et al. [41])

The lung is another complex organ comprising more than 40 various cell lineages, which produce strong background during fluorescence imaging. Several stem cell niches have been identified in terminal bronchioles or bronchoalveolar junctions [44]. Lung stem cells (LSCs) are responsible for epithelial repair as well as tissue homeostasis, and are able to renew and proliferate to form epithelial cells in vivo. To enable the therapeutic applications of LSCs, it is crucial to determine their tissue-specific engraftment [45] and regenerative capacity [46] in animals. Recently, Chang's group has successfully demonstrated the homing property of LSCs by using the FND labeling technique [47]. Compared to organic dye and fluorescent proteins (with low transfection efficiency) which are susceptible to photobleaching and interfere with the tissue autofluorescence, FND serves as a highly photostable imaging probe that enable long-term tracking of the FND labeled cells in vivo. The authors also showed that LSCs can be spontaneously labeled with FNDs by endocytosis, and the labeling did not affect cellular functions. By combining FND labeling with FLIM technique, they were able to identify transplanted cells in histological lung sections after intravenous (i.v.) injection of the FND-labeled LSCs into mice for more than a week, with single-cell resolution. More importantly, the authors applied lung injury mice to investigate the tissue-specific engraftment capacity of LSCs.

In vivo stem cell tracking was tested in healthy normal mice and injured mice respectively. Firstly, about 5×10^5 FND-labeled LSCs were injected into the tail veins of the healthy mice. Cells in lungs, kidneys, liver and spleen were collected on days 1, 4 and 7 after injection [47]. By gating the fluorescence signal at 9 ns, the authors could readily distinguish the background noises from the FND fluorescence signals. Hence, the location of FND-labeled LSCs could be clearly revealed (Fig. 8). Due to the photostability, of the NV fluorophores, the authors further confirmed that FNDs with prolonged excitation did not result in any significant decrease in fluorescence intensity. It is demonstrated that the FND-labeled LSCs in the mice could be tracked for 7 days after i.v. injection.

It is known that the regenerative capacity of LSCs is determined both by their intrinsic developmental potential and their interaction with other cell elements in their niches [46]. This capacity could be significantly activated after tissue injury. To illustrate this effect, the authors tracked LSCs in lung-injured mice. In this experiment, 5×10^5 FND-labeled LSCs were injected into the mice after lung injury for 2 days. The extent of the injury and the repair of the bronchiolar epithelium could be examined by immunostaining against club cell secretory protein (CCSP) [48], which was expressed by LSCs. Further analysis for the H&E staining bright image and the corresponding time-gated fluorescence (τ = 9–18 ns) image revealed that the FND-labeled LSCs were preferentially localized in the terminal bronchioles of the lung-injured mice (Fig. 9), in contrast to the localization of the cells in the subepithelium of bronchiolar airways in uninjured mice (Fig. 8). Our results showed that the lung epithelia of the injured mice were restored more rapidly after transplantation of the FND-labeled LSCs than with saline control (Fig. 9). The authors also found that the percentage of the transplanted LSCs engrafted to the lung was estimated to be $\sim$23 % on Day 1, and the percentage

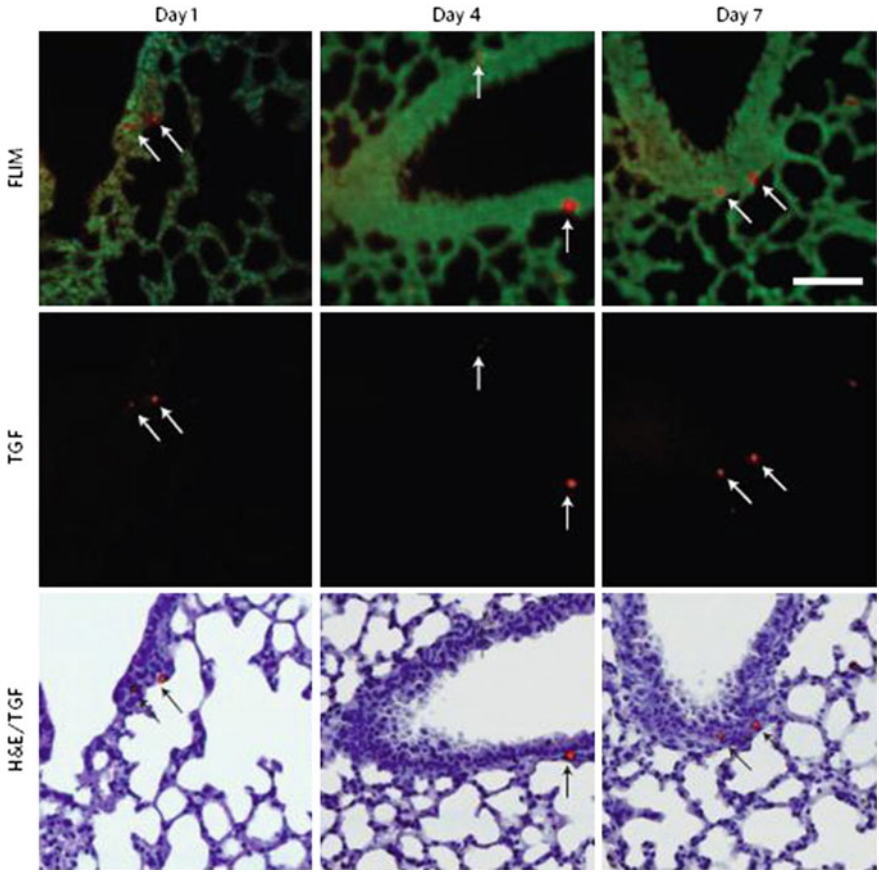

Fig. 8 FND-labeled LSCs in uninjured mice on different days. Representative FLIM, TGF and bright-field H&E staining images of the same lung tissue sections from uninjured mice. The merged H&E and TGF images in the *last row* show that the FND-labelled cells (denoted by *black arrows*) are primarily located in the subepithelium of bronchiolar airways. Scale bar = 50 μm. (Reprinted from Wu et al. [47])

markedly declined to 1.7 % on day 7 (Fig. 8). In contrast, the percentage of the transplanted LSCs engrafted to the lung for the lung injury model exhibited a much smaller decrease, with the percentage of 13 % on day 1 and 11 % on Day 7 (Fig. 9). The distinct contrast between these two results confirms that the homing phenomenon of the transplanted FND-labeled cells in the injury models is a 'pro-active' tissue-specific engraftment, instead of non-specific or passive entrapment [47].

In addition, to examine whether the FND-labeled LSCs engrafted in lung were viewed as foreign substances in the living system and engulfed by macrophages

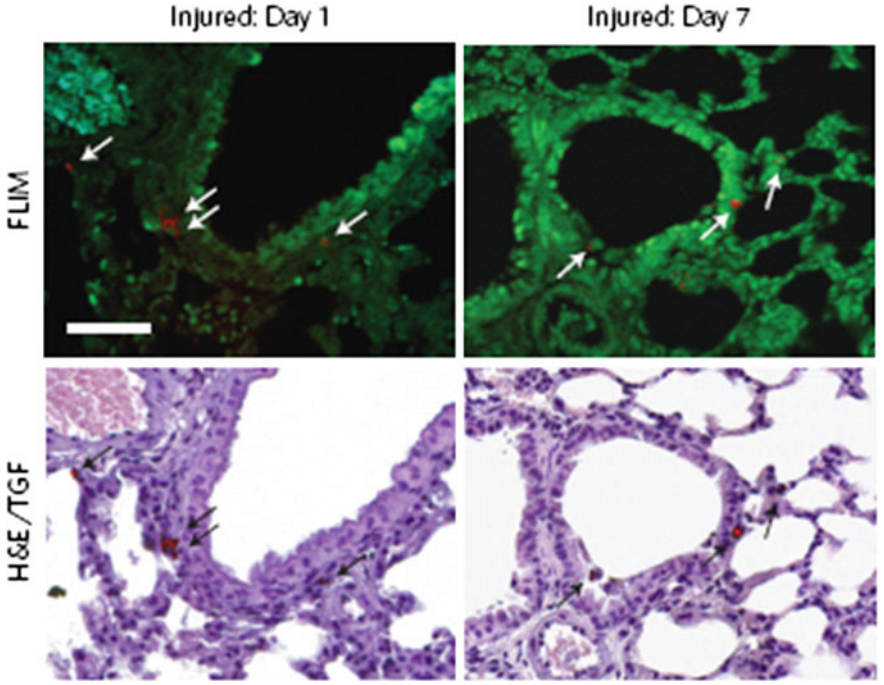

Fig. 9 FND-labeled LSCs in lung-injured mice on different days. Representative FLIM, TGF and bright-field H&E staining images of the same lung tissue sections, showing the location of FND-labeled LSCs (denoted by *white and black arrows*) in terminal bronchioles of the lungs. Scale bar = 50 μm. (Reprinted from Wu et al. [47])

through a process called "phagocytosis" [49], Chang's group stained the lung tissue sections with the macrophage-specific antibody, F4/80. They further did haematoxylin and eosin (H&E) staining and the fluorescence imaging. Overlapping of the bright-field and time-gated fluorescence images (Fig. 10) showed no sign of FND co-localization with the F4/80-stained macrophages, which excluded the possibility that the observed FND-labeled LSCs were phagocytosed after i.v. injection. It should be noted that such identification could not been made with organic dyes such as carboxyfluorescein succinimidyl ester (CFSE), because the lifetimes for the CFSE and the background fluorescence were similar.

In this work, Chang's group demonstrated that the FND labeling technique enables quantitative assessment of the distribution of transplanted LSCs in tissue, due to the excellent chemical stability and photostability of the nanomaterial. Additionally, the FND-labeled cells could be counted visually from the images. Although the mechanism how the injected LSCs reach lung tissues and further engraft to the terminal bronchioles are not yet fully understood, the results support

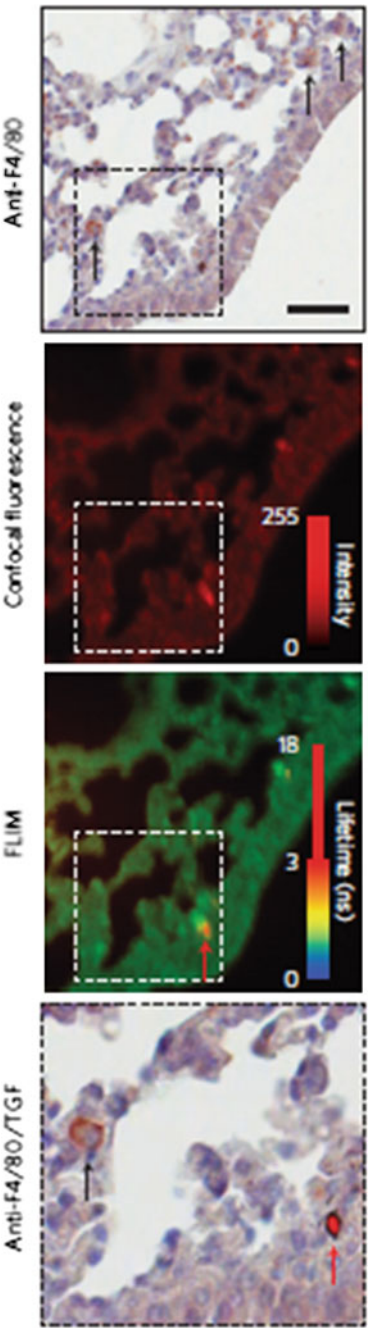

Fig. 10 Colocalization examination of FND-labeled LSCs and macrophages in a lung tissue section immunostained with macrophage-specific antigen F4/80 and H&E staining. The enlarged view shows that the transplanted FND-labeled cells (*red* and indicated by *red arrows*) and alveolar macrophages (*brown* and indicated by *black arrows*) are located at different positions. Scale bar = 10 μm. (Reprinted from Wu et al. [47])

that specific microenvironments (or niches) in lungs plays an important role in the regulation of tissue-specific engraftment, structural support and the signals for self-renewal and differentiation of the stem cells [47].

Most recently, Hui et al. presented another approach to achieve in vivo background-free fluorescence imaging of FNDs by an intensified charge-coupled device (ICCD) as the detector. ICCD is useful to suppress short-lifetime autofluorescence backgrounds and provide time-gated fluorescence images with high contrast [50]. With ICCD and a Raman shifter, the authors demonstrated the first application for wide-field fluorescence imaging of the FND-labeled cells in living animals. The authors labeled mouse lung cancer cells with FNDs and then introduced 1×10^5 labeled cells into a mouse via tail vein injection. Then, fluorescence imaging was carried out in a main blood vessel of the mouse ear. Figure 11a, b are bright-field and time-gated fluorescence images of the ear tissue respectively. About 10 min after intravenous injection of the FND-labeled lung cancer cells into the mouse, bright moving objects with an average speed of 0.4 μm/s could be clearly identified in the blood vessel at a frame rate of 2 Hz (Fig. 11c). It is noted that this measured speed was much lower than the blood flow velocity by about 3 orders of magnitude, and thus most likely associated with rolling, instead of flowing, of the FND-labeled cells in the blood vessel. The technique provides real-time imaging and tracking of transplanted stem cells in tissue repair and regeneration in vivo. Also, the real-time tracking of FND-labeled cancer cells during metastasis in vivo is plausible. The next interesting issue is the application of FND for in vivo study of circulating tumor cells in blood [51]. It is deemed feasible in the near future with FNDs conjugated with bioactive ligands or grafted with high-specificity antibodies against tumor-specific biomarkers through biotin-avidin interactions [52].

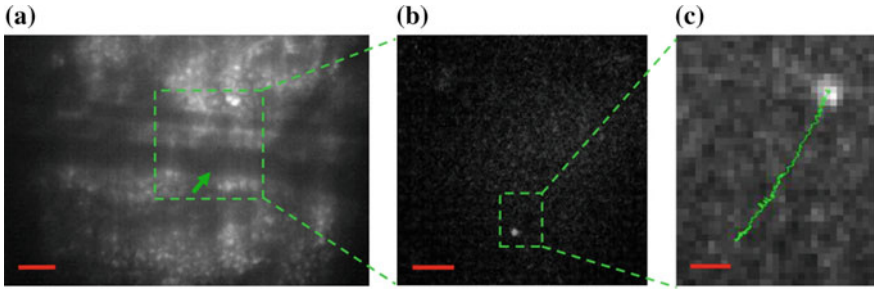

Fig. 11 **a** Bright-field image of a mouse ear tissue. The *green arrow* indicates the position of an FND-labeled lung cancer cell in the blood vessel of ~50 μm in diameter. **b** Enlarged view of the fluorescence image of the *square green* region in **a**. The *bright spot* corresponds to the FND-labeled lung cancer cell. **c** Enlarged view of the fluorescence image of the *rectangular green* region in **b**, showing the trajectory of the FND-labeled lung cancer cell moving in the vessel. The average speed of the cell movement is 0.4 μm/s. The frame rate is 2 Hz and the objective lens is 10×. The red scale bar corresponds to 100, 50, and 10 μm in **a**, **b** and **c**, respectively. (Reprinted from Hui et al. [50])

3.3 Superresolution Imaging

One of the unique feature for FND is its perfect photostability, which provides an excellent fluorophore for superresolution imaging like stimulated emission depletion (STED) microscopy [53–58], saturated excitation (SAX) microscopy [59], localization microscopy [60], Deterministic emitter switch microscopy (DESM) [61] and scanning near field microscopy [62–64] and Dual-point illumination AND-gate microscopy [65]. We focus on STED and SAX, which have already been reported for bio-imaging.

The STED microscopy utilizes two laser beams at different wavelengths [66]. The main laser beam brings the fluorophore of interest to its excited state. The second laser beam, also called the STED beam, de-excites the fluorophore from the excited state to the ground state through stimulated emission processes. The STED beam has a doughnut shape which excites the outer region around the focus. During imaging, the fluorescence of the emitter excited by the main laser stays unaffected in the center of the doughnut spot but diminishes at the outer ring. Compared to the other superresolution techniques, STED microscopy does not require any mathematical post-processing. Accordingly, it is most suitable for high-resolution imaging of biological cells in real time and three dimensions. Tzeng et al. has taken advantage of the FND photostability, and applied STED to study FND labeling for HeLa cells [55]. To prevent agglomeration in cell medium, FND particles of 30 nm in size were first coated non-covalently with bovine serum albumin (BSA) and then delivered to the cell cytoplasm by endocytosis. With the green light for the excitation and a doughnut-shaped 740-nm laser beam for the depletion, the authors were able to achieve a resolution close to 40 nm. They identified the individual FND particles in cells and distinguished them from FND aggregates trapped in endosomes. Prabhakar et al. applied STED to study the endosome merging into late endosomes and estimate the drug load taken up by an individual cell [56].

SAX microscopy exploits the nonlinear fluorescence response, when the fluorophore is intensely illuminated. The excellent photostability of the NV^- center in FNDs enables SAX microscopy to achieve superresolution bioimaging without photobleaching problems, even under intense light illumination [59]. To investigate cellular processes like intracellular transport and cellular uptake, Yamanaka et al. demonstrated three-dimensional high-resolution imaging of FNDs distributed in a macrophage cell by SAX microscopy. Compared with the confocal image for FNDs, SAX image significantly improves the spatial resolution, which enables more accurate measurement of the FND distribution in the macrophage cell after intracellular transport.

3.4 Multiphoton Excitation Microscopy

FND tracking in biological tissue still presents challenging, because the tissue components are extremely heterogeneous and scatter light severely [67]. The strong

scattering of the various tissue components has restricted high-resolution optical imaging to the skin surface. Multiphoton excitation microscopy excites the sample with infrared light and offers an attractive alternative to reduce the tissue scattering. As the infrared light scatters in tissue much weaker than the visible light, the multiphoton microscopy has a longer penetration depth to provide better optical sectioning for thick tissue than the one-photon counterpart. Moreover, the multiphoton absorption cross section is typically small and the excitation power density has to be high. Hence, the MPE is spatially confined to the vicinity of the focal spot which reduces the out-of-focus excitation and also the photo-damage to cells. Two-photon microscopy has already been demonstrated to improve the image contrast of FND in cellular level [25, 68]. We anticipate that multiphoton excitation microscopy can be applicable for FND tracking (about few mm) below the skin surface.

3.5 *Tissue Imaging with Microwave Modulation Only*

Utilizing the spin properties of the NV^- center, Igarashi et al. have established a selective imaging protocol to improve the image contrast of FNDs in vitro and in vivo, because the fluorescence of FND can also be darkened by the microwave at 2.87 GHz [69]. The NV^- center of in a FND particle has a triplet ground state with the $m_s = 0$ sublevel and the $m_s = \pm 1$ sublevel. When there is no external magnetic field, the zero-field energy splitting between the $m_s = 0$ and $m_s = \pm 1$ sublevel is 2.87 GHz, which corresponds to the microwave frequency. In this protocol, the microwave turns on and is resonant with the transition, the electron population in the triplet ground state will shift from the $m_s = 0$ to the $m_s = \pm 1$. The population in the $m_s = \pm 1$ sublevel has higher probability to go to the intermediate state than the $m_s = 0$ sublevel, and then return to the $m_s = 0$ sublevel via non-radiative decay. Hence, when the microwave turns from off to on, the FND signal will decrease, from bright to dark. In this protocol, the wide-field fluorescence images were first recorded with or without the microwave irradiation at 2.87 GHz (Fig. 12). Then the

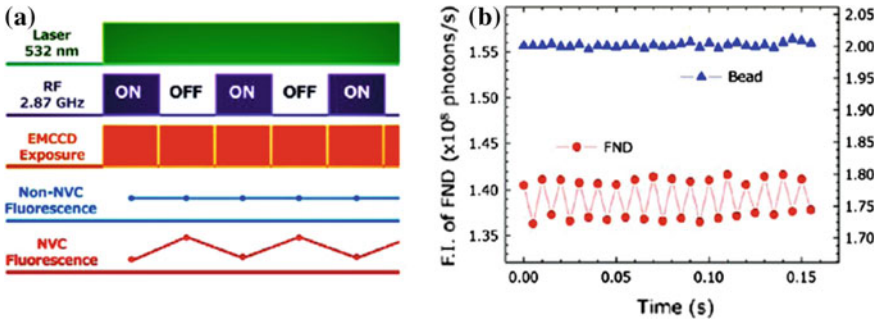

Fig. 12 **a** Time chart of the laser excitation, microwave irradiation and image acquisition, along with the expected intensity profiles of non-NV and NV fluorescence used for selective imaging of FNDs. **b** Time trace of the observed fluorescence intensities of FNDs and fluorescent beads. (Reprinted from Igarashi et al. [69])

subtraction between these two images at every pixel was carried out to yield selective images of the FND particles. Since the alternative microwave irradiation modulated only the fluorescence intensity of the NV^- centers, the subtraction between these two images effectively removed autofluorescence background signals of the specimen and thus significantly improved the image contrast. The protocol was shown applicable to a wide variety of living systems from single cells to whole animals like *Caenorhabditis elegans* [70] and mice.

3.6 Tissue Imaging with Magnetic Field Modulation Only

Apart from a microwave, a magnetic field can also decrease the fluorescence intensity of FND, because a magnetic field mixes NV center's spin sublevels and eliminate the selectivity of intersystem crossing [71]. (The mechanism for FND darkening by magnetic field is different from the microwave in the previous subsection.) When the NV center undergoes continuous excitation without magnetic field, the intersystem crossing from the singlet state to the $m_s = 0$ sublevel of the ground state is dominant than the $m_s = \pm 1$ sublevels. Hence the NV center is polarized under continuous excitation and the bright state is predominately occupied. However, if the NV center undergoes continuous excitation in the presence of magnetic field, the intersystem crossing rate becomes approximately equal for all three sublevels. The NV center loses its spin-polarizability and has higher probability for non-radiative transition. Thus, FNDs in the presence of magnetic field appear 10–20 % darker in the absence of magnetic field, and the fluorescence intensity of FND is dependent on the magnetic field. Using image subtraction method [71], the magnetic-independent background can be eliminated, leaving the background-free FND signals. Chapman et al. observed FND in vitro with strong autofluorescence background and improved the image contrast by this image subtraction method. Sarkar et al. injected silica-coated FNDs in the front foot pad of intact mice and imaged sentinel lymph nodes. The FND particles were drained to the proximal auxiliary sentinel Lymph Nodes in Fig. 13, and the FND signal were further enhanced by computational lock-in detection [72].

3.7 Tissue Imaging Combining Microwave and Quadruple Coils

Most recently, Hegyi et al. applied the ODMR technique for high-resolution imaging of FNDs in tissue with a magnetic quadruple coil (Fig. 14) [73, 74]. Magnetic fields completely cancel at the center of the imaging system, where are

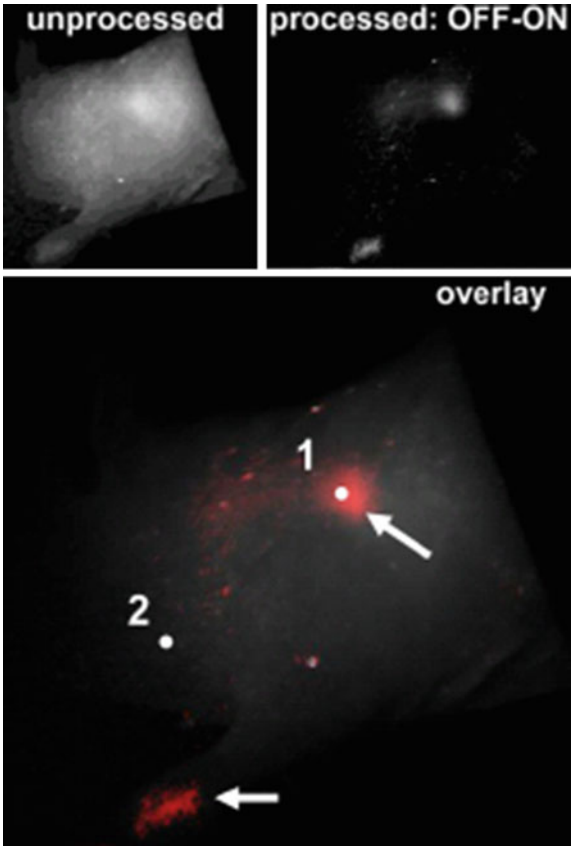

Fig. 13 In vivo imaging of sentinel lymph nodes of a mouse with FND. The mouse is obtained by pairwise subtracting with and without the magnetic field, and averaged with 475 images. The processed image (*top right inset*, *red* in *overlay*) was overlaid on an unprocessed image obtained with the magnetic field off (*top left inset*, *white* in *overlay*). The *white arrows* point to the injection site in the footpad and the location of the auxiliary lymph node. Signal from the FNDs in the lymph node is clearly detected. (Reprinted from Sarkar et al. [72])

called field-free line [73]. Only at this field-free line, FND will resonate with the microwave at 2.87 GHz. In other region with non-vanishing magnetic field, the FND will not resonate with 2.87 GHz because the resonance frequency of the transition is split by the magnetic field. Thus, in the presence of this microwave, which is turned on and off periodically, the variation in the fluorescence intensity, which is further measured with a lock-in amplifier, is proportional to the FND concentration at the field-free region. So the authors swept this field-free point across a region and record the intensities with the microwave on and off respectively. The intensity difference would then correspond to FND concentration at the field-free point. A quantitative map of FND concentration was then generated. This technique vastly improves the resolution in deep tissue optical imaging. They imaged large letter written by FND coated tape under 5 mm chicken breast [73].

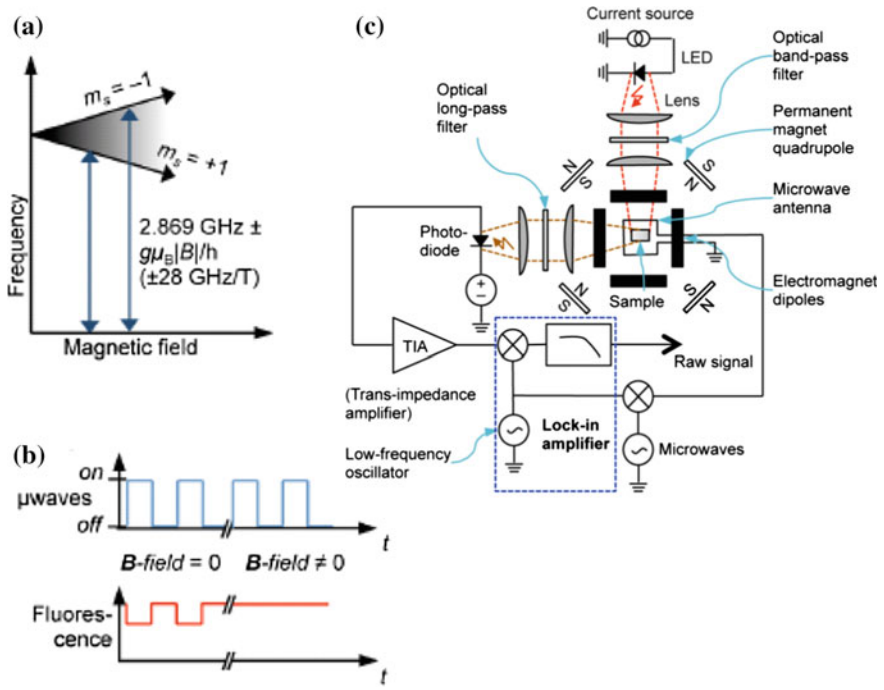

Fig. 14 Schematic diagram of an imaging system for NV^- centers in FNDs based on ODMR detection. **a** At zero magnetic field, spin transition frequency is 2.869 GHz. The upper spin sublevels split with increasing magnetic field. **b** With $|B| = 0$, turning on microwave at 2.869 GHz decreases the observed fluorescence from FND. In a strong B-field ($|B| > 0$), the microwave does not modulate the fluorescence. **c** "Magnetic well" created by the quadruple coils, with non-vanishing magnetic field everywhere except at the center of imaging system. Adapted with the permission of [73]. (Reprinted from Hegyi et al. [73])

4 Emerging Technologies for Quantum Sensing

4.1 Magnetic Field Sensor

The NV^- center has a magnetically sensitive triplet ground state. The unperturbed electronic energy structure of the center consists of a triplet ground state with the $m_s = 0$ sublevel and $m_s = \pm 1$ sublevel. The latter two sublevels are degenerate at zero external magnetic field, and are energetically higher than the $m_s = 0$ sublevel by a crystal field splitting of 2.87 GHz. When an external magnetic field is applied to the center, the field will split the $m_s = \pm 1$ sublevels and the ODMR spectrum of the NV^- center will change accordingly. Hence, an NV^- center is magnetically sensitive and applicable as a magnetic probe. Gruber, et al. demonstrated that the ODMR spectrum of a single NV^- center can be optically read out at the single molecule level. The sublevel population of the triplet ground state can

be inferred from the change in the fluorescence signal between the $^3A_2$ and ^3E transition. This unique spin system, combined with the ODMR technique, suggests ultrasensitive and rapid detection of single electronic spin states under ambient conditions, for nanoscale magnetic resonance imaging. Balasubramanian et al. incorporated a nanodiamond hosting a single nitrogen-vacancy center into a cantilever of an atomic force microscope, and further applied the cantilever with the ODMR setup as a scanning probe magnetometer to achieve subwavelength imaging resolution [75].

Rondin et al. reported nanoscale magnetic imaging with a similar nanodiamond probe which is all-optical and sensitive to large off-axis magnetic fields. Most importantly, it does not require microwave control therefore extends the operation range of diamond-based magnetometry [76]. A few research groups have also applied nanodiamond to detect single spin as well as weak magnetic field, and their outstanding works for high resolution magnetometry have been elaborated in a recent review [3, 77]. Most recently Horowitz et al. have applied an infrared laser as an optical tweezer for the three dimensional control of the FND particle in liquid solution [78]. Then the crystal field splitting of the NV^- centers in the FND particle was read out by simultaneous application of a green laser and microwave. As the applied frequency was tuned across 2.87 GHz, the fluorescence intensity showed a significant decrease ($\sim$10 %). Hence, the optically trapped FNDs enable three-dimensional mapping of the magnetic fields in solution in Fig. 15, and probing of the magnetic fields in complex environments like the interiors of microfluidic

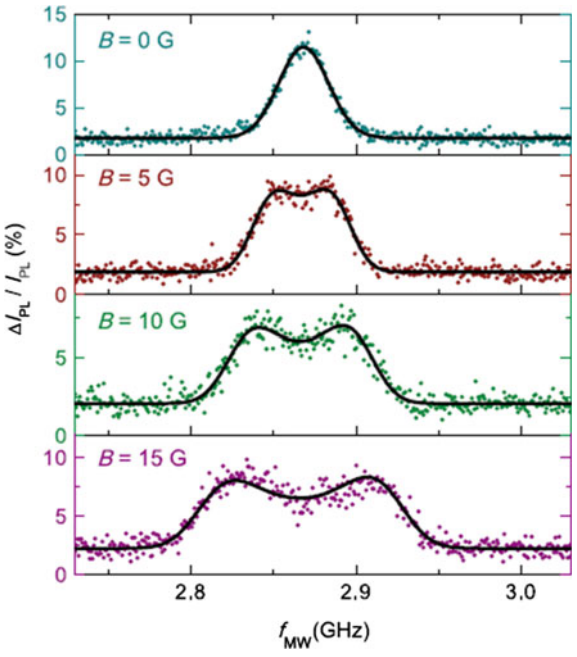

Fig. 15 ODMR spectra of trapped nanodiamond ensembles at calibrated low field strengths. The ODMR measurements are taken at the calibrated applied magnetic fields of 0 G, 5 G, 10 G and 15 G respectively. (Reprinted from Horowitz et al. [78])

channels. Geiselmann et al. have also shown the deterministic trapping and three-dimensional spatial manipulation of individual NDs hosting NV centers for local magnetic field measurement [79].

4.2 Orientation Tracker for NV Axis

The diamond crystal field separates the $m_s = 0$ sublevel of the ground state from the degenerate $m_s = \pm 1$ sublevel by 2.87 GHz. Furthermore, the energy splitting depends on the angle between the NV axis and an external magnetic field. Hence, a single NV^- center can act as an intrinsic compass under the magnetic field. McGuinness et al. can identify the orientation of the NV axis by applying the microwave field to examine the energy splitting of the FND hosting a single NV^- center [80, 81]. They further applied a uniform magnetic field to live HeLa cells to measure the peak positions of the ODMR spectra and successfully resolved the rotational motion of a FND particle in the cell at the millisecond timescale. The orientation of the NV^- center was continuously monitored for more than 16 h in a HeLa cell.

4.3 Nano-Thermometry [82]

The crystal field splitting of the NV^- center depends on the thermally induced lattice strains [83–89]. FND can be applied as a nanoscale thermometer. There have been currently two method to measure the local temperature, ODMR [89] and all-optical detection [90]. Kucsko et al. introduced both nanodiamonds and gold nanoparticles into a single human embryonic fibroblast, and demonstrated temperature control and mapping at the subcellular level. Combining ODMR setup, a few research groups also applied FND particles for nanoscale temperature sensing. On the other hand, Plakhotnik et al. has shown an all-optical technique to extract the same temperature information [90]. The method exploited the temperature dependence of NV^- center's optical Debye-Waller factor. In short, they measured the visible ZPL of the NV^- center and deduced the temperature. The accuracy of the all-optical thermometry is 0.3 K.

4.4 Nanoscopic Spin Probe

Kaufmann et al. have applied a single NV^- center in a nanodiamond to detect gadolinium (Gd) spin labels in an artificial cell membrane under ambient conditions [91]. The Gd^{3+} ion, a common magnetic resonance imaging contrast agent with spin 7/2, labels the lipid molecules in a supported lipid bilayer. The Gd-labeled lipid

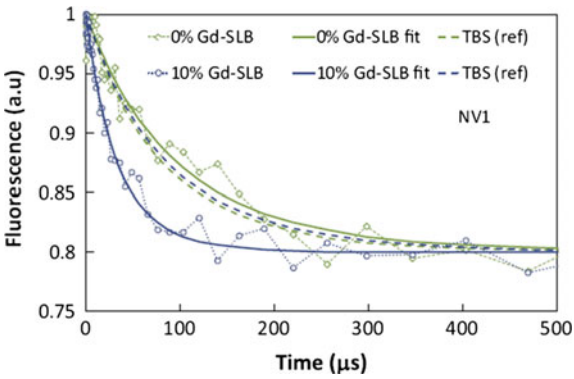

Fig. 16 Detection of spin-labeled lipids in a supported lipid bilayer (SLB) using the relaxation time T_1 of single NV^- spins in nanodiamonds. Relaxation of the spin of a single NV^- center in a nanodiamond in a SLB without spin labels (*green*) and in a SLB with 10 % Gd spin labels (*blue*). (Reprinted from Kaufmann et al. [91])

molecules produces characteristic magnetic fluctuations in the artificial membrane, by cross-lipid Gd–Gd spin dipole interactions, motional diffusion of individual Gd-labeled lipids and intrinsic Gd spin relaxation effects. Kaufmann et al. monitored the relaxation time T_1 of the single NV^- center in the lipid bilayer by optically polarizing the $m_s = 0$ state and then measuring the probability P(t) of finding the NV^- in the $m_s = 0$ state at a later time. The relaxation time is shortened when the artificial membrane is labeled with 10 % Gd spin-labeled lipids in Fig. 16. The average reduction in the T_1 relaxation time from the reference value is 74 ± 6 % and hence the nanodiamond probe is sensitive to near individual (4 ± 2) proximal Gd labels.

Meanwhile, Ermakova et al. demonstrated that single nanodiamond hosting multiple NV^- centers can also detect individual ferritin molecules [92]. (Ferritin has a small fraction of uncompensated Fe^{3+} spin with a magnetic moment of 300 μ_B. The ferritin concentration in blood serum is correlated with the total amount of iron stored in the body.) They first attached the ferritin molecules to the surface of the FND by non-covalent binding to the amino groups of the nanodiamond, and hence produced diamond-ferritin complexes. Then they compared the relaxation time T_1 between the free nanodiamond and the diamond-ferritin complex, and observed a significant decline of the relaxation time for the free nanodiamond. (Compared with current magnetic force microscopy techniques, these nanodiamond probes do not require cryogenic temperature and vacuum.) The successful detection for such small numbers of spins opens a pathway for in situ detection nanoscale detection of dynamical processes in biology.

5 Conclusions and Perspectives

NV^- center in nanodiamond has unique optical properties (like photostability and biocompatibility) as well as spin properties. It is also shown that FND particles could be conjugated with biomolecules which enable FND to serve as a vehicle for drug

and gene delivery [52]. Thus FND have been successfully applied for bio-imaging and quantum sensing in the past ten year. There are a few challenges ahead. For example, real-time three-dimensional tracking in deep tissue with better fluorescence image contrast is one of the challenges for bio-imaging. Combining ODMR technique and multiphoton microscopy offer a possible solution for high-resolution optical imaging under the skin [74]. Apart from NV center, there are potential color centers in nanodiamond for bioimaging. For example, the silicon-vacancy center has narrow near infrared emission at 739 nm with full width at half maximum of 4 nm [35], and its magnetic property is still under investigation [93].

It is also anticipated the NV^- center hosting in nanodiamond finds more biological applications for quantum sensing in the near future, because the ODMR spectrum is sensitive to the variation of magnetic field, electric field, temperature and pressure. The NV^- center in nanodiamond has been already operated with the microwave excitation and developed as a nanoprobe for local temperature and magnetic field measurement respectively. To extend the operation range in the biomedical field, it is necessary to develop the FND as an all-optical nanoprobe without the microwave excitation [90]. In summary, we foresee that the applications of FND are going to create more breakthroughs in bioimaging and quantum sensing.

References

1. R. Schirhagl, K. Chang, M. Loretz, C.L. Degen, Nitrogen-vacancy centers in diamond: nanoscale sensors for physics and biology. Annu. Rev. Phys. Chem. **65**, 83–105 (2014). doi:10.1146/annurev-physchem-040513-103659
2. C. Bradac, T. Gaebel, J.R. Rabeau, Nitrogen-vacancy color centers in diamond: properties, synthesis, and applications. in *Optical Engineering of Diamond*, First edn. ed by R.P. Mildren, J.R. Rabeau. (Boschstr. 12, 69496, Wiley-VCH Verlag GmbH & Co. KGaA., Weinheim, Germany, 2013). doi: 10.1002/9783527648603.ch5
3. L. Rondin, J.P. Tetienne, T. Hingant, J.F. Roch, P. Maletinsky, V. Jacques, Magnetometry with nitrogen-vacancy defects in diamond. Rep. Prog. Phys. **77**, 056503 (2014). doi:10.1088/0034-4885/77/5/056503
4. Y.Y. Hui, H.C. Chang, Recent developments and applications of nanodiamonds as versatile bioimaging agents. J. Chin. Chem. Soc. **161**, 67–76 (2014). doi:10.1002/jccs.201300346
5. V.N. Mochalin, O. Shenderova, D. Ho, Y. Gogotsi, The properties and applications of nanodiamonds. Nat. Nanotechnol. **7**, 11–23 (2012). doi:10.1038/nnano.2011.209
6. J.R. Maze, A. Gali, E. Togan, Y. Chu, A. Trifonov, E. Kaxiras, M.D. Lukin, *Properties of nitrogen vacancy centers in diamond: the group theoretic approach* (Phys, New J, 2011). doi:10.1088/1367-2630/13/2/025025
7. L. Rondin, G. Dantelle, A. Slablab, F. Grosshans, F. Treussart, P. Bergonzo, S. Perruchas, T. Gacoin, M. Chaigneau, H.C. Chang, V. Jacques, J.F. Roch, Surface-induced charge state conversion of nitrogen-vacancy defects in nanodiamonds. Phys. Rev. B **82**, 115449 (2010). doi:10.1103/PhysRevB.82.115449
8. K.-M.C. Fu, C. Santori, P.E. Barclay, R.G. Beausoleil, Conversion of neutral nitrogen-vacancy centers to negatively charged nitrogen-vacancy centers through selective oxidation. Appl. Phys. Lett. **96**, 121907 (2010). doi:10.1063/1.3364135

9. C.C. Fu, H.Y. Lee, K. Chen, T.S. Lim, H.Y. Wu, P.K. Lin, P.K. Wei, P.H. Tsao, H.C. Chang, W. Fann, Characterization and application of single fluorescent nanodiamonds as cellular biomarkers. Proc. Natl. Acad. Sci. U.S.A. **104**, 727–732 (2007). doi:10.1073/pnas.0605409104
10. V. Vaijayanthimala, Y.K. Tzeng, H.C. Chang, C.L. Li, The biocompatibility of fluorescent nanodiamonds and their mechanism of cellular uptake. Nanotech. **20**, 425103 (2009). doi:10.1088/0957-4484/20/42/425103
11. N. Mohan, C.S. Chen, H.H. Hsieh, Y.C. Wu, H.C. Chang, In vivo imaging and toxicity assessments of fluorescent nanodiamonds in *Caenorhabditis elegans*. Nano Lett. **10**, 3692–3699 (2010). doi:10.1021/nl1021909
12. V. Vaijayanthimala, P.Y. Cheng, S.H. Yeh, K.K. Liu, C.H. Hsiao, J.I. Chao, H.C. Chang, The long-term stability and biocompatibility of fluorescent nanodiamond as an in vivo contrast agent. Biomater. **33**, 7794 (2012). doi:10.1016/j.biomaterials.2012.06.084
13. D. Passeri, F. Rinaldi, C. Ingallina, M. Carafa, M. Rossi, M.L. Terranova, C. Marianecci, biomedical applications of nanodiamonds: an overview. J Nanosci Nanotech. **15**(2), 972–988 (2015). doi:10.1166/jnn.2015.9734
14. V.M. Acosta, A. Jarmola, E. Bauch, D. Budker, Optical properties of the ntrogen-vacancy singlet levels in diamond. Phys. Rev. B **82**, 201202 (2010). doi:10.1103/PhysRevB.82.201202
15. M.W. Doherty, N.B. Manson, P. Delaney, F. Jelezko, J. Wrachtrup, L.C. Hollenberg, The nitrogen vacancy colour centre in diamond. Phys. Rep. **528**, 1–45 (2013). doi:10.1016/j.physrep.2013.02.001
16. A. Gruber, A. Drabenstedt, C. Tietz, L. Fleury, J. Wrachtrup, C. von Borczyskowski, Scanning Confocal Optical Microscopy and Magnetic Resonance on Single Defect Centers. Sci. **276**, 2012–2014 (1997). doi:10.1126/science.276.5321.2012
17. N.B. Manson, J.P. Harrison, M.J. Sellars, Nitrogen-vacancy center in diamond: model of the electronic structure and associated dynamics. Phy. Rev B **74**, 104303 (2006). doi:10.1103/PhysRevB.74.104303
18. F. Jelezko, J. Wrachtrup, Single defect centres in diamond: a review. Phys. Stat. Solidus A **203**, 3207–3225 (2006). doi:10.1002/pssa.200671403
19. A. Beveratos, R. Brouri, T. Gacoin, J.P. Poizat, P. Grangier, Nonclassical radiation from diamond nanocrystals. Phys. Rev. A **64**, 061802 (2002). doi:10.1103/PhysRevA.64.061802
20. S.J. Yu, M.W. Kang, H.C. Chang, K.M. Chen, Y.C. Yu, Bright fluorescent nanodiamonds: no photobleaching and low cytotoxicity. J. Am. Chem. Soc. **127**, 17604–17605 (2005). doi:10.1021/ja0567081
21. O. Faklaris, D. Garrot, V. Joshi, F. Druon, J.P. Boudou et al., Detection of single photoluminescent diamond nanoparticles in cells and study of the internalization pathway. Small **4**, 2236–2239 (2008). doi:10.1002/smll.200800655
22. J. Tisler, G. Balasubramanian, B. Naydenov, R. Kolesov, B. Grotz et al., Fluorescence and spin properties of defects in single digit nanodiamonds. ACS Nano **3**, 1959–1965 (2009). doi:10.1021/nn9003617
23. N. Mohan, Y.K. Tzeng, L. Yang, Y.Y. Chen, Y.Y. Hui, C.Y. Fang, H.C. Chang, Sub-20 nm fluorescent nanodiamonds as photostable biolabels and fluorescence resonance energy transfer donors Adv. Mater. **21**, 1–5 (2010). doi:10.1002/adma.200901596
24. J. Havlik, V. Petrakova, I. Rehor, V. Petrak, M. Gulka et al., Boosting nanodiamond fluorescence: towards development of brighter probes. Nanoscale **5**, 3208–3211 (2013). doi:10.1039/C2NR32778C
25. Y.R. Chang, H.Y. Lee, K. Chen, C.C. Chang, D.S. Tsai, C.C. Fu, T.S. Lim, Y.K. Tzeng, C.Y. Fang, C.C. Han, H.C. Chang, W. Fann, Mass production and dynamic imaging of fluorescent nanodiamonds *Nat*. Nanotech. **3**, 284–288 (2008). doi:10.1038/nnano.2008.99
26. C. Bradac, G. Torsten, N. Naidoo, J.R. Rabeau, A.S. Barnard, Prediction and measurement of the size-dependent stability of fluorescence in diamond over the entire nanoscale. Nano Lett. **9**, 3555–3564 (2009). doi:10.1021/nl9017379

27. B.R. Smith, D.W. Inglis, B. Sandnes, J.R. Rabeau, A.V. Zvyagin, D. Gruber, C.J. Noble, R. Vogel, E. Osawa, T. Plakhotnik, Five-nanometer diamond with luminescent nitrogen-vacancy defect centers. Small **5**(14), 1649–1653 (2009). doi:10.1002/smll.200801802
28. J.P. Boudou, P.A. Curmi, F. Jelezko, J. Wrachtrup, P. Aubert, M. Sennour, G. Balasubramanian, R. Reuter, A. Thore, E. Gaffet, High yield fabrication of fluorescent nanodiamonds. Nanotechnology **20**, 235602 (2009). doi:10.1088/0957-4484/20/23/235602
29. J.P. Boudou, J.J. Tisler, R. Reuter, A. Thorel, P.A. Curmi, F. Jelezko, J. Wrachtrup, Fluorescent nanodiamonds derived from HPHT with a size of less than 10 nm. Diam. Relat. Mater. **37**, 80–86 (2013). doi:10.1016/j.diamond.2013.05.006
30. B.R. Smith, D. Gruber, T. Plakhotnik, The effects of surface oxidation on luminescence of nanodiamonds. Diam. Relat. Mater. **19**, 314–318 (2010). doi:10.1016/j.diamond.2009.12.009
31. T. Gaebel, C. Bradac, J. Chen, J.M. Say, L. Brown, P. Hemmer, J.R. Rabeau, Size-reduction of nanodiamonds via air oxidation. Diam. Relat. Mater. **21**, 28–32 (2012). doi:10.1016/j.diamond.2011.09.002
32. J.R. Rabeau, A. Stacey, A. Rabeau, S. Prawer, F. Jelezko, I. Mirza, J. Wrachtrup, Single nitrogen vacancy centers in chemical vapor deposited diamond nanocrystals. Nano Lett. **7**, 3433–3437 (2007). doi:10.1021/nl0719271
33. J. Michl, T. Teraji, S. Zaiser, I. Jakobi, G. Waldherr, F. Dolde, P. Neumann, M.W. Doherty, N. B. Manson, J. Isoya, J. Wrachtrup, Perfect alignment and preferential orientation of nitrogen-vacancy centers during chemical vapor deposition diamond growth on (111) surfaces. Appl. Phys. Lett. **104**, 102407 (2014). doi:10.1063/1.4868128
34. A.M. Edmonds, U.F.S. D'Haenens-Johansson, R.J. Cruddace, M.E. Newton, K.-M.C. Fu, C. Santori, R.G. Beausoleil, D.J. Twitchen, M.L. Markham, Production of oriented nitrogen-vacancy color centers in synthetic diamond. Phy. Rev. B **86**, 035201 (2012). doi:10.1103/PhysRevB.86.035201
35. I. Aharonovich, Diamond nanocrystals for photonics and sensing. J.J. Appl. Phys. **53**(5), 05FA01 (2014). doi.:10.7567/JJAP.53.05FA01
36. Y.C. Lin, E. Perevedentseva, L.W. Tsai, K.T. Wu, C.L. Cheng, Nanodiamond for intracellular imaging in the microorganisms in vivo. J. Biophotonics **5**, 838–847 (2012). doi:10.1002/jbio.201200088
37. E. Perevedentseva, Y.C. Lin, M. Jani, C.L. Cheng, Biomedical applications of nanodiamonds in imaging and therapy. Nanomed. **8**(12), 2041–2060 (2013). doi:10.2217/nnm.13.183
38. T. C. Hsu, K. K. Liu, H. C. Chang, E. Hwang, J. I. Chao, Labeling of neuronal differentiation and neuron cells with biocompatible fluorescent nanodiamonds. Sci. Rep. 4 (2014). doi: 10.1038/srep05004
39. O. Faklaris, J. Botsoa, T. Sauvage, J.F. Roch, F. Treussart, Photoluminescent nanodiamonds: comparison of the photoluminescence saturation properties of the NV color center and a cyanine dye at the single emitter level, and study of the color center concentration under different preparation conditions. Diam. Relat. Mater. **19**(7–9), 988–995 (2010). doi:10.1016/j.diamond.2010.03.002
40. C.Y. Fang, V. Vaijayanthimala, C.A. Cheng, S.H. Yeh, C.F. Chang, C.L. Li, H.C. Chang, The exocytosis of fluorescent nanodiamond and its use as a long-term cell tracker. Small **7**(23), 3363–3370 (2011). doi:10.1002/smll.201101233
41. Y. Kuo, T.Y. Hsu, Y.C. Wu, H.C. Chang, Fluorescent nanodiamond as a probe for the intercellular transport of proteins in vivo. Biomat. **34**, 8352–8360 (2013). doi:10.1016/j.biomaterials.2013.07.043
42. D.A. Simpson, A.J. Thompson, M. Kowarsky, N.F. Zeeshan, M.S.J. Barson, L.T. Hall, Y. Yan, S. Kaufmann, B.C. Johnson, T. Ohshima, F. Caruso, R.E. Scholten, R.B. Saint, M. J. Murray, L.C.L. Hollenberg, In vivo imaging and tracking of individual nanodiamonds in drosophila melanogaster embryos. Biomed. Opt. Exp. **5**(4), 1250–1261 (2014). doi:10.1364/BOE.5.001250
43. C. Kurtsiefer, S. Mayer, P. Zarda, H. Weinfurter, Stable solid-state source of single photons. Phys. Rev. Lett. **85**(2), 290–293 (2000). doi:10.1103/PhysRevLett.85.290

44. A. Giangreco, S.D. Reynolds, B.R. Stripp, Terminal bronchioles harbor a unique airway stem cell population that localizes to the bronchoalveolar duct junction. Am. J. Pathol. **161**, 173–182 (2002). doi:10.1016/S0002-9440(10)64169-7
45. D.A. Chistiakov, Endogenous and exogenous stem cells: a role in lung repair and use in airway tissue engineering and transplantation. J. Biomed. Sci. **17**, 92 (2010). doi:10.1186/1423-0127-17-92
46. A.N. Lau, M. Goodwin, C.F. Kim, D.J. Weiss, Stem cells and regenerative medicine in lung biology and diseases. Mol. Ther. **20**, 1116–1130 (2012). doi:10.1038/mt.2012.37
47. T.J. Wu, Y.K. Tzeng, W.W. Chang, C.A. Cheng, Y. Kuo, C.H. Chien, H.C. Chang, J. Yu, Tracking the engraftment and regenerative capabilities of transplanted lung stem cells using fluorescent nanodiamonds. Nature Nanotech. **8**, 682–689 (2013). doi:10.1038/nnano.2013.147
48. B.R. Stripp, K. Maxson, R. Mera, G. Singh, Plasticity of airway cell proliferation and gene expression after acute naphthalene injury. Am. J. Physiol. Lung Cell Mol. Physiol. **269**, L791–L799 (1995)
49. M. Jonathan, Austyn and Siamon Gordon, F4/80, a monoclonal antibody directed specifically against the mouse macrophage. Eur. J. Immunol **11**, 805–815 (1981). doi:10.1002/eji.1830111013
50. Y.Y. Hui, L.J. Su, O.Y. Chen, Y.T. Chen, T.M. Liu, H.C. Chang, Wide-field imaging and flow cytometric analysis of cancer cells in blood by fluorescent nanodiamond labeling and time gating. Sci. Rep. **4**, 5574 (2014). doi:10.1038/srep05574
51. E. Galanzha, E.V. Shashkov, T. Kelly, J.W. Kim, L. Yang, V.P. Zharov, In vivo magnetic enrichment and multiplex photoacoustic detection of circulating tumour cells. Nat. Nanotech. **4**, 855–860 (2009). doi:10.1038/NNANO.2009.333
52. B.M. Chang, H.H. Lin, L.J. Su, W.D. Lin, R.J. Lin, Y.K. Tzeng, R.T. Lee, Y.C. Lee, A.L. Yu, H.C. Chang, Highly fluorescent nanodiamonds protein-functionalized for cell labeling and targeting. Adv. Funct. Mater. **23**, 5737–5745 (2013). doi:10.1002/adfm.201301075
53. K.Y. Han, K.I. Willig, E. Rittweger, F. Jelezko, C. Eggeling, S.W. Hell, Three-Dimensional stimulated emission depletion microscopy of nitrogen-vacancy centers in diamond using continuous-wave light. Nano Lett. **9**, 3323–3329 (2009). doi:10.1021/nl901597v
54. Y.K. Tzeng, O. Faklaris, B.M. Chang, Y. Kuo, J.H. Hsu, H.C. Chang, Superresolution imaging of albumin-conjugated fluorescent nanodiamonds in cells by stimulated emission depletion. Angew. Chem. Int. Ed. **50**, 2262 (2011). doi:10.1002/anie.201007215
55. N. Prabhakar, T. Näreoja, E. von Haartman, D.Ş. Karaman, H. Jiang, S. Koho, T.A. Dolenko, P.E. Hänninen, D.I. Vlasov, V.G. Ralchenko, S. Hosomi, I.I. Vlasov, C. Sahlgrenbci, J.M. Rosenholm, Core–shell designs of photoluminescent nanodiamonds with porous silica coatings for bioimaging and drug delivery II: application. Nanoscale **5**, 3713–3722 (2013). doi:10.1039/c3nr33926b
56. N.D. Lai, O. Faklaris, D. Zheng, V. Jacques, H.C. Chang, J.F. Roch, F. Treussart, Quenching nitrogen–vacancy center photoluminescence with an infrared pulsed laser. New J. Phys. **15**, 033030 (2013). doi:10.1088/1367-2630/15/3/033030
57. S. Arroyo-Camejo, M.P. Adam, M. Besbes, J.P. Hugonin, V. Jacques, J.J. Greffet, J.F. Roch, S.W. Hell, F. Treussart, Stimulated emission depletion microscopy resolves individual nitrogen vacancy centers in diamond nanocrystals. ACS Nano **7**, 10912–10919 (2013). doi:10.1021/nn404421b
58. X. Yang, Y.K. Tzeng, Z. Zhu, Z. Huang, X. Chen, Y. Liu, H.C. Chang, L. Huang, W.D. Li, P. Xi, Sub-diffraction imaging of nitrogen-vacancy centers in diamond by stimulated emission depletion and structured illumination. RSC Adv. **4**(11305–11310), 2014 (2014). doi:10.1039/c3ra47240j
59. M. Yamanaka, Y.K. Tzeng, S. Kawano, N.I. Smith, S. Kawata, H.C. Chang, K. Fujita, SAX microscopy with fluorescent nanodiamond probes for high-resolution fluorescence imaging. Biomed. Optics Exp. **2**, 1946–1954 (2011). doi:10.1364/BOE.2.001946
60. M. Gu, Y. Cao, S. Castelletto, B. Kouskousis, X. Li, Super-resolving single nitrogen vacancy centers within single nanodiamonds using a localization microscope. Opt. Exp. **21**(15), 17639–17646 (2013). doi:10.1364/OE.21.017639

61. E.H. Chen, O. Gaathon, M.E. Trusheim, D. Englund, Wide-field multispectral super-resolution imaging using spin-dependent fluorescence in nanodiamonds. Nano Lett. **13**, 2073–2077 (2013). doi:10.1021/nl400346k
62. Y.Y. Hui, Y.C. Lu, L.J. Su, C.Y. Fang, J.H. Hsu, H.C. Chang, Tip-enhanced sub-diffraction fluorescence imaging of nitrogen-vacancy centers in nanodiamonds. Appl. Phys. Lett. **102**, 013102 (2013). doi:10.1063/1.4773364
63. R. Beams, D. Smith, T.W. Johnson, S.H. Oh, L. Novotny, A.N. Vamivakas, Nanoscale fluorescence lifetime imaging of an optical antenna with a single diamond NV center. Nano Lett. **13**(8), 3807–3811 (2013). doi:10.1021/nl401791v
64. A.W. Schell, P. Engel, J.F.M. Werra, C. Wolff, K. Busch, O. Benson, Scanning single quantum emitter fluorescence lifetime imaging: quantitative analysis of the local density of photonic states. Nano lett. **14**(5), 2623–2627 (2014). doi:10.1021/nl500460c
65. J. Kwon, Y. Lim, J. Jung, S.K. Kim, New sub-diffraction-limit microscopy technique: dual-point illumination AND-gate microscopy on nanodiamonds. Opt Exp **20**, 13347–13356 (2014). doi:10.1364/OE.20.013347
66. G. Vicidomini, G. Moneron, K.Y. Han, V. Westphal, H. Ta, M. Reuss, J. Engelhardt, C. Eggeling, S.W. Hell, Sharper low-power, STED nanoscopy by time gating. Nat. Meth. **8**, 571–575 (2011). doi:10.1038/nmeth.1624
67. F. Helmchen1, W. Denk, Deep tissue two-photon microscopy. Nat. Meth. **2**(12), 932–940 (2005). doi:10.1038/NMETH818 2 photon review
68. Y.Y. Hui, B. Zhang, Y.C. Chang, C.C. Chang, H.C. Chang, J.H. Hsu, K. Chang, F.H. Chang, Two-photon fluorescence correlation spectroscopy of lipid-encapsulated fluorescent nanodiamonds in living cells. Optics Express **18**, 5896–5905 (2010). doi:10.1364/OE.18.005896
69. R. Igarashi, Y. Yoshinari, H. Yokota, T. Sugi, F. Sugihara, K. Ikeda, H. Sumiya, S. Tsuji, I. Mori, H. Tochio, Y. Harada, M. Shirakawa, Real-time background-free selective imaging of fluorescent nanodiamonds in Vivo. Nano Lett. **12**, 5726–5732 (2012). doi:10.1021/nl302979d
70. Y. Yoshinari, S. Mori, R. Igarashi, T. Sugi, H. Yokota, K. Ikeda, H. Sumiya, I. Mori, H. Tochio, Y. Harada, M. Shirakawa, Optically detected magnetic resonance of nanodiamonds in vivo; implementation of selective imaging and fast sampling. J. Nanosci. Nanotechnol **15**, 1014–1021 (2015). doi:10.1166/jnn.2015.9739
71. R. Chapman, T. Plakhoitnik, Background-free imaging of luminescent nanodiamonds using external magnetic field for contrast enhancement. Optics Lett. **38**(11), 1847–1849 (2013). doi:10.1364/OL.38.001847
72. S.K. Sarkar, A. Bumb, X. Wu, K.A. Sochacki, P. Kellman, M.W. Brechbiel, K.C. Neuman, Wide-field in vivo background free imaging by selective magnetic modulation of nanodiamond fluorescence. Biomed. Opt. Exp. **5**, 1190–1202 (2014). doi:10.1364/BOE.5.001190
73. A. Hegyi, E. Yablonovitch, Molecular imaging by optically detected electron spin resonance of nitrogen-vacancies in nanodiamonds. Nano. Lett. **13**, 1173 (2013). doi:10.1021/nl304570b
74. A. Hegyi, E. Yablonovitch, Nanodiamond molecular imaging with enhanced contrast and expanded field of view. J. Biomed. Opt. **19**, 011015 (2014). doi: 10.1117/1.JBO.19.1.011015
75. G. Balasubramanian, I.Y. Chan, R. Kolesov, M. Al-Hmoud, J. Tisler et al., Nanoscale imaging magnetometry with diamond spins under ambient conditions. Nature **455**, 648–651 (2008). doi:10.1038/nature07278
76. L. Rondin, J.P. Tetienne, P. Spinicelli, C. Dal Savio, K. Karrai, G. Dantelle, A. Thiaville, S. Rohart, J.F. Roch, V. Jacques, Nanoscale magnetic field mapping with a single spin scanning probe magnetometer. Appl. Phys. Lett. **100**, 153118 (2012). doi:10.1063/1.3703128
77. J.M. Taylor, P. Cappellaro, L. Childress, L. Jiang, D. Budker, P.R. Hemmer, A. Yacoby, R. Walsworth, M.D. Lukin, High-sensitivity diamond magnetometer with nanoscale resolution. Nat. Phy. **4**, 810–816 (2008). doi:10.1038/nphys1075
78. V. R. Horowitz, B. J. Alemán, D. J. Christle, A. N. Cleland, D. D. Awschalom, Electron spin resonance of nitrogen-vacancy centers in optically trapped nanodiamonds. Proc. Nat. Acad. Sci. USA, **109**, 13493 (2012). doi:10.1073/pnas.1211311109M

79. M.L. Geiselmann, J. Juan, J.M. Renger, L.J. Say, F.J.G. de Brown, F. Abajo, R. Koppens, Quidant, three-dimensional optical manipulation of a single electron spin. Nat. Nantech. **8**, 175–179 (2013). doi:10.1038/nnano.2012.259
80. L.P. McGuinness, Y. Yan, A. Stacey, D.A. Simpson, L.T. Hall et al., Quantum measurement and orientation tracking of fluorescent nanodiamonds. Nat. Nanotechnol. **6**, 358–363 (2011). doi:10.1038/nnano.2011.64
81. D. Maclaurin, L.T. Hall, A.M. Martin, L.C.L. Hollenberg, Nanoscale magnetometry through quantum control of nitrogen–vacancy centres in rotationally diffusing nanodiamonds. New J. Phys. **15**, 013041 (2013). doi:10.1088/1367-2630/15/1/013041
82. G. Baffou, H. Rigneault, D. Marguet, L. Jullien, A critique of methods for temperature imaging in single cells. Nat. Meth. **11**(9), 899–901 (2014). doi:10.1038/nmeth.3073
83. V.M. Acosta, E. Bauch, M.P. Ledbetter, A. Waxman, L.S. Bouchard, D. Budker, Temperature dependence of the nitrogen-vacancy magnetic resonance in diamond. Phys. Rev. Lett. **104**, 070801 (2010). doi:10.1103/PhysRevLett.104.070801
84. T. Plakhotnik, D. Gruber, Luminescence of nitrogen-vacancy centers in nanodiamonds at temperatures between 300 and 700 K: perspectives on nanothermometry. Phys. Chem. Chem. Phys. **12**, 9751–9756 (2010). doi:10.1039/c001132k
85. X.D. Chen, C.H. Dong, F.W. Sun, C.L. Zou, J.M. Cui et al., Temperature dependent energy level shifts of nitrogen-vacancy centers in diamond. Appl. Phys. Lett. **99**, 161903 (2011). doi:10.1063/1.3652910
86. D.M. Toyli, D.J. Christle, A. Alkauskas, B.B. Buckley, C.G. van de Walle, D.D. Awschalom, Measurement and control of single nitrogen-vacancy center spins above 600 K. Phys. Rev. X **2**, 031001 (2012). doi:10.1103/PhysRevX.2.031001
87. P. Neumann, I. Jakobi, F. Dolde, C. Burk, R. Reuter et al., High-precision nanoscale temperature sensing using single defects in diamond. Nano Lett. **13**, 2738–2742 (2013). doi:10.1021/nl401216y
88. D.M. Toyli, C.F. de las Casas, D.J. Christle, V.V. Dobrovitski, D.D. Awschalom, Fluorescence thermometry enhanced by the quantum coherence of single spins in diamond. Proc. Natl. Acad. Sci. USA **110**, 8417–8421 (2013). doi:10.1073/pnas.1306825110
89. G. Kucsko, P.C. Maurer, N.Y. Yao, M. Kubo, H.J. Noh, P.K. Lo, H. Park, M.D. Lukin, Nanometer scale quantum thermometry in a living cell. Nature **500**, 54–58 (2013). doi:10.1038/nature12373
90. T. Plakhotnik, M.W. Doherty, J.H. Cole, R. Chapman, N.B. Manson, All-optical thermometry and thermal properties of the optically detected spin resonances of the NV–center in nanodiamond. Nano Lett. **14**, 4989–4996 (2014). doi:10.1021/nl501841d
91. S. Kaufmann, D.A. Simpson, L.T. Hall, V. Perunicic, P. Senn, S. Steinertf, L.P. McGuinnessa, B.C. Johnsong, T. Ohshimag, F. Carusod, J. Wrachtrup, R.E. Scholtenh, P. Mulvaney, L. Hollenberg, Detection of atomic spin labels in a lipid bilayer using a single-spin nanodiamond probe. Proc. Natl. Acad. Sci. USA **110**, 10894–10898 (2013). doi:10.1073/pnas.1300640110
92. A. Ermakova, G. Pramanik, J. Cai, G. Algara-Siller, U. Kaiser, T. Weil, Y.K. Tzeng, H.C. Chang, L.P. McGuinness, M.B. Plenio, B. Naydenov, F. Jelezko, Detection of a few metallo-protein molecules using color centers in nanodiamonds. Nano Lett. **13**, 3305–3309 (2013). doi:10.1021/nl4015233
93. C. Hepp, T. Müller, V. Waselowski, J.N. Becker, B. Pingault, H. Sternschulte, D. Steinmüller-Nethl, A. Gali, J.R. Maze, M. Atatüre, C. Becher, Electronic structure of the silicon vacancy color center in diamond. Phys. Rev. Lett. **112**, 036405 (2014). doi:10.1103/PhysRevLett.112.036405